Research Square

Preprints are preliminary reports that have not undergone peer review.
They should not be considered conclusive, used to inform clinical practice,
or referenced by the media as validated information.

# Targeting the CHD3 Chromatin Remodeler Exploits a Synthetic Lethal Vulnerability in SWI/SNF-Deficient Cancers via Toxic Derepression of PARD3B

**Mariko Takeuchi**
National Cancer Center Research Institute
**Yoshie Okimoto**
National Cancer Center Research Institute
**Makoto Fukushima**
National Cancer Center Research Institute
**Harumi Hirano**
National Cancer Center Research Institute
**Hideaki Ogiwara**
hogiwara@ncc.go.jp

National Cancer Center Research Institute

**Article**

**Keywords:** SWI/SNF deficiency, CHD3, Synthetic lethality, PARD3B, Chromatin remodeling, Epigenetic therapy, MYC signaling

**Posted Date:** March 2nd, 2026

**DOI:** https://doi.org/10.21203/rs.3.rs-8811494/v1

**License:** This work is licensed under a Creative Commons Attribution 4.0 International License.
Read Full License

**Additional Declarations:** Competing interest reported. H.O. received research grants from Ono Pharmaceutical Co., Ltd. during the conduct of the study. The other authors declare no competing interests.

**Version of Record:** A version of this preprint was published at npj Precision Oncology on May 22nd, 2026. See the published version at https://doi.org/10.1038/s41698-026-01499-7.

# Abstract

SWI/SNF-deficient cancers characterized by dual SMARCA4/SMARCA2 loss, including undifferentiated thoracic sarcomas and subsets of lung adenocarcinoma, represent a major therapeutic challenge. While paralog-targeting strategies exist for single-subunit loss, dual-deficient tumors lack actionable targets. Here, we identify the CHD3/NuRD nucleosome remodeling complex as a critical synthetic lethal vulnerability in these malignancies. Through an integrated genomic analysis, we demonstrate that in the absence of SWI/SNF, CHD3 acts as an essential "epigenetic brake" at the enhancer of the cell polarity regulator PARD3B. Loss of CHD3 triggers aberrant chromatin hyper-accessibility and toxic derepression of PARD3B. We further elucidate that PARD3B accumulation drives cell death by inducing the "functional uncoupling" of MYC signaling. This occurs via spatial perturbation of upstream signaling hubs, which silences MYC transcriptional output without degrading the protein itself. Therapeutically, CHD3 depletion led to robust tumor regression in SWI/SNF-deficient xenografts, validating the mechanism of PARD3B upregulation and the collapse of the MYC pathway in vivo. Our study defines a novel mode of synthetic lethality driven by "gain-of-toxicity" rather than loss of survival signals, uncovering a fatal cross-complex dependency. We propose that targeting CHD3 to unleash PARD3B toxicity offers a promising therapeutic avenue for treatment-refractory SWI/SNF-deficient cancers.


# Significance

**Dual SMARCA4/SMARCA2 loss creates a fatal dependency on CHD3. CHD3 suppression triggers toxic PARD3B derepression, collapsing MYC signaling through functional uncoupling. This identifies a novel vulnerability for treatment-refractory malignancies.**

# Introduction

Mutations in genes encoding the SWI/SNF (BAF) chromatin remodeling complex are identified in over 20% of human cancers, constituting a major class of oncogenic drivers [1]. Among these, "SWI/SNF-deficient cancers," characterized by the concurrent loss of the ATPase subunit SMARCA4 (BRG1) and its paralog SMARCA2 (BRM), or the complete loss of core subunits, encompass highly aggressive malignancies such as small cell carcinoma of the ovary, hypercalcemic type (SCCOHT), thoracic SMARCA4-deficient undifferentiated tumors, malignant rhabdoid tumors, and a subset of lung adenocarcinomas [2–5]. These malignancies maintain an undifferentiated state due to profound epigenetic dysregulation and are largely refractory to conventional chemotherapies [6,7]. Consequently, the establishment of novel therapeutic strategies targeting specific vulnerabilities arising from SWI/SNF deficiency remains an urgent clinical priority [6,7].

To address this challenge, extensive efforts have been made to identify therapeutic targets exploiting the concept of synthetic lethality. To date, promising strategies include the inhibition of the antagonistic methyltransferase EZH2 [8] and the degradation or inhibition of the residual paralog SMARCA2 [9–11]. Recently, we also reported the efficacy of inhibiting the histone acetyltransferases CBP/p300 in specific

SWI/SNF-deficient contexts [12,13]. However, a critical limitation exists: therapeutic strategies targeting SMARCA2, while effective in *SMARCA4*-single-deficient cancers, are inherently inapplicable to *SMARCA4*/*SMARCA2* dual-deficient malignancies that lack the target paralog entirely.

Chromatin architecture is maintained through the coordinated action of diverse ATP-dependent remodeling complexes, including not only SWI/SNF but also ISWI, CHD, and INO80 families [14]. Whether cancer cells that have completely lost SWI/SNF—the primary regulatory machinery—acquire a lethal dependency on these "alternative chromatin remodeling complexes" to maintain genomic homeostasis remains largely unexplored, and the molecular mechanisms underlying such potential dependencies are unknown.

CHD3 (Chromodomain Helicase DNA Binding Protein 3) is a core ATPase subunit of the Nucleosome Remodeling and Deacetylase (NuRD) complex, forming a unique assembly that couples ATP-dependent nucleosome remodeling with histone deacetylation activities [15,16]. Although the NuRD complex has traditionally been viewed as a transcriptional repressor, recent studies suggest a context-dependent role in transcriptional activation, indicating functional pleiotropy [17]. However, the specific role of CHD3 in supporting cancer cell survival within the aberrant chromatin landscape of SWI/SNF deficiency remains entirely unelucidated.

In this study, through a comprehensive screen of chromatin remodeling factors in *SMARCA4*/*SMARCA2* dual-deficient cancer cells, we identified CHD3 as a novel synthetic lethal target. We demonstrate that in the absence of SWI/SNF, CHD3 functions as an essential "epigenetic brake" that maintains chromatin compaction at the locus of the cell polarity regulator *PARD3B*. Strikingly, we reveal that CHD3 loss triggers aberrant hyper-accessibility and transcriptional derepression of the *PARD3B* enhancer. The resulting toxic accumulation of PARD3B induces cell death via the "functional uncoupling" of the MYC signaling pathway. This study elucidates a fatal interdependency between distinct chromatin remodeling complexes and provides *in vivo* proof-of-concept for CHD3-targeted therapy as a promising strategy for treatment-refractory SWI/SNF-deficient malignancies.

## Results

# CHD3 is a Specific Synthetic Lethal Vulnerability in SWI/SNF-Deficient Cancers

To identify novel dependencies in SWI/SNF-deficient cancers, particularly those harboring dual deficiency of SMARCA4 and SMARCA2, we established an isogenic cell model using the SMARCA4/SMARCA2-deficient H23 lung cancer cell line and its SMARCA4-restored counterpart (Fig. 1A). We performed an siRNA screen targeting 17 ATP-dependent chromatin remodeling factors outside the SWI/SNF complex. This screen identified CHD3, SMARCA1, and SMARCA5 as candidates exhibiting significant lethality in SWI/SNF-deficient cells (Fig. 1B).

Next, we validated these candidates using SWI/SNF-proficient (PC9, H2228, ES-2) and SWI/SNF-deficient (H23, H1703, TOV112D) cell lines **(**Fig. 1C**)**. While depletion of SMARCA1 and SMARCA5 exhibited no toxicity toward SWI/SNF-proficient cells, depletion of CHD3, a core ATPase of the NuRD complex, induced selective lethality in SWI/SNF-deficient lines without affecting proficient lines **(**Fig. 1D**)**.

To further verify this selective dependency, we utilized the H23 isogenic model. Knockdown of CHD3 in the parental SMARCA4/SMARCA2-deficient H23 cells markedly reduced cell viability, whereas this lethality was significantly rescued in SMARCA4-restored H23 cells **(**Fig. 1E-F; **Expression data in Supplementary Fig. 1A)**.

To generalize these findings, we assembled a broad panel of cell lines comprising SMARCA4/SMARCA2-proficient (n = 8), dual-deficient (n = 5), and SMARCA4-single-deficient (n = 4) lines to evaluate CHD3 dependency **(**Fig. 1G, **Supplementary Fig. 1B)**. CHD3 knockdown had minimal effect on the survival of proficient lines but significantly reduced the viability of dual-deficient lines **(**Fig. 1H-I, **Supplementary Fig. 1C-D)**. Interestingly, While survival of CHD3 knockdown in SMARCA4-single-deficient lines was significantly reduced compared to proficient lines, its effect was intermediate compared to dual-deficient lines **(**Fig. 1H**)**. These results suggest that dual deficiency of SMARCA4 and SMARCA2, rather than SMARCA4 loss alone, is a critical determinant of synthetic lethal dependency on CHD3.

We confirmed the robustness of CHD3 dependency using distinct siRNA sequences, which reproduced specific lethality in dual-deficient lines (H1703, H23, SBC-5) while sparing proficient cells (H460) **(Supplementary Fig. 1E-F)**. Similarly, sustained CHD3 knockdown using a doxycycline-inducible shRNA system showed minimal effects on proficient H460 cells **(Supplementary Fig. 1G-H)** but induced progressive and significant viability loss in dual-deficient H23 cells **(Supplementary Fig. 1I-J)**.

In the H23 isogenic model, SMARCA4 restoration resulted in a slight decrease in *CHD3* mRNA levels **(Supplementary Fig. 1K)**; however, across the cell line panel, no clear correlation was observed between SWI/SNF mutation status and *CHD3* expression levels **(Supplementary Fig. 1L)**. This suggests that the dependency of SWI/SNF-deficient cancers on CHD3 reflects a functional addiction rather than mere overexpression.

Finally, to determine whether this synthetic lethal interaction is specific to CHD3 within the NuRD complex, we screened other NuRD subunits in H23 cells. Depletion of subunits other than CHD3 (e.g., MBD2, MTA families) did not elicit potent and selective lethal effects **(**Fig. 1J**)**. Collectively, these data indicate that SWI/SNF-deficient cancers possess a specific and fatal dependency on the CHD3 remodeling ATPase among NuRD complex components.

## Toxic Overexpression of PARD3B Drives CHD3 Synthetic Lethality

As a core component of the NuRD chromatin remodeling complex, CHD3 regulates the transcription of various genes. We hypothesized that in SWI/SNF-deficient cancers (SMARCA4-/SMARCA2-), CHD3 suppression induces synthetic lethality through the aberrant expression of specific CHD3 target genes.

To identify the causative gene determining this synthetic lethality, we employed an integrated analysis combining RNA-sequencing (RNA-seq) for comprehensive gene expression profiling and ATAC-sequencing (ATAC-seq) for chromatin accessibility profiling **(**Fig. 2A, **Left Panel)**.

First, using the SWI/SNF-deficient H23 isogenic cell model, we identified differentially expressed genes (DEGs) upon CHD3 knockdown. We detected 829 DEGs in H23 Mock (SMARCA4-deficient) cells and 1,015 DEGs in H23 + SMARCA4 (restored) cells (fold change > 2). Among these, 556 genes were differentially expressed specifically in H23 Mock cells. In parallel, ATAC-seq analysis identified 1,715 and 1,698 altered chromatin peaks (fold change > 2) in H23 Mock and H23 + SMARCA4 cells, respectively. Notably, 1,376 peaks were specifically altered in H23 Mock cells, corresponding to 1,280 genes located in the vicinity of these peaks. By intersecting the mock-specific DEGs with genes exhibiting mock-specific chromatin alterations, we narrowed down the candidates to 28 genes that exhibited transcriptional dysregulation potentially driven by chromatin structural changes in their regulatory regions.

To further refine these candidates for universality across cancer types, we performed RNA-seq analysis on panels of lung and ovarian cancer cell lines **(**Fig. 2A, **Right Panel)**. Comparing SWI/SNF-deficient lung cancer cells (H1703) with proficient cells (H2009), we identified 939 and 596 DEGs, respectively, with 824 genes specifically altered in the deficient line. Similarly, in ovarian cancer models, comparing deficient cells (TOV112D) with proficient cells (ES-2) revealed 1,265 and 731 DEGs, respectively, with 1,121 genes specifically altered in the deficient line. Intersection of the deficient-specific DEGs from both lung and ovarian models yielded 192 common genes.

Strikingly, PARD3B was identified as the sole candidate gene shared between the 28 genes from the isogenic model and the 192 genes from the cell line panels. PARD3B is a scaffold protein known to regulate cell polarity and tight junction formation, although its role in cancer cell survival is context-dependent [18]. Validation by RT-qPCR confirmed that robust induction of *PARD3B* mRNA upon CHD3 depletion occurred specifically in SWI/SNF-deficient cell lines **(**Fig. 2B**)**.

To determine whether PARD3B induction is the direct driver of synthetic lethality in SWI/SNF-deficient cells, we performed rescue experiments using simultaneous knockdown. In SWI/SNF-deficient lung (H23, H1703) and ovarian (TOV112D) cancer cell lines, CHD3 knockdown reduced *CHD3* mRNA **(**Fig. 2C, **Supplementary Fig. 2A)** and led to a marked increase in *PARD3B* mRNA **(**Fig. 2D, **Supplementary Fig. 2B)** and protein **(**Fig. 2E-F**)** levels, resulting in significant cell viability loss **(**Fig. 2G, **Supplementary Fig. 2C)**. However, simultaneous knockdown of CHD3 and PARD3B significantly, and in some cases remarkably, rescued the lethality observed with CHD3 single knockdown **(**Fig. 2G, **Supplementary Fig. 2C)**. These results demonstrate that the observed synthetic lethality is driven by the toxic overexpression of PARD3B rather than the loss of CHD3 function per se.

Given that the CHD3/NuRD complex contains histone deacetylases (HDAC1 and HDAC2) as core subunits, we investigated whether deacetylase activity is required for CHD3-mediated repression of *PARD3B*. We treated SWI/SNF-deficient cell lines (H23, H1703, and TOV112D) with the pan-HDAC

inhibitor Vorinostat. The response was heterogeneous: while *PARD3B* expression increased in TOV112D cells, it decreased in H1703 cells and remained unchanged in H23 cells (Figure S2D). These findings suggest that the repressive function of CHD3 at the *PARD3B* locus is not solely dependent on HDAC1/2 enzymatic activity, implying that the structural integrity or nucleosome remodeling capacity of the NuRD complex is critical for this regulation.

**CHD3 Functions as an Epigenetic Brake at the PARD3B Enhancer**

We next investigated how CHD3 regulates *PARD3B* expression. In SMARCA4-restored H23 cells, CUT&RUN sequencing revealed that CHD3 occupies both promoter (co-localizing with H3K4me3/H3K27ac) and enhancer (co-localizing with H3K4me1/H3K27ac) regions genome-wide **(Supplementary Fig. 3A)**. Notably, CHD3 exhibited a strong tendency to co-localize with SMARCA4, particularly at enhancer regions **(Supplementary Fig. 3A)**. Detailed inspection of the *PARD3B* locus in SMARCA4-restored H23 cells revealed that CHD3 and SMARCA4 co-localize at multiple putative enhancer regions (E1, E2, E3) rather than the promoter region **(**Fig. 3A**)**. Importantly, CHD3 occupancy at these regions was maintained even in the absence of SMARCA4 (H23 Mock). To assess chromatin accessibility, we performed ATAC-seq. In SWI/SNF-deficient H23 cells, CHD3 knockdown led to a marked increase in chromatin accessibility (ATAC signal) at *PARD3B* enhancers, most prominently at the E1 region located on the 5' side of the gene **(**Fig. 3B**)**. Similarly, in other SWI/SNF-deficient cells (H1703, TOV112D), CHD3 depletion induced a significant gain of chromatin accessibility at the 5' region of the *PARD3B* locus **(Supplementary Fig. 3B)**. These findings indicate that in the absence of SWI/SNF, CHD3 acts as an essential "epigenetic brake" to maintain a closed chromatin state at the *PARD3B* locus, preventing its transcriptional derepression.

## PARD3B Accumulation Drives Functional Uncoupling of MYC Signaling

To investigate the mechanisms by which CHD3 suppression and PARD3B overexpression induce cell death in SWI/SNF-deficient cells, we sought to identify common molecular pathways enriched in the altered gene signatures. Gene Set Enrichment Analysis (GSEA) revealed that *HALLMARK_MYC_TARGETS_V1* and *V2* signatures were commonly suppressed by both CHD3 knockdown and PARD3B overexpression in SWI/SNF-deficient cells **(**Fig. 4A–E, **Supplementary Fig. 4A–G)**. Conversely, comparisons between SWI/SNF-deficient and -proficient cell lines revealed that MYC target signatures were significantly enriched in SWI/SNF-deficient cells **(**Fig. 4F–G, **Supplementary Fig. 4H–J)**. This suggests that while SWI/SNF-deficient cells are inherently addicted to hyperactive MYC signaling, PARD3B accumulation following CHD3 suppression potently abrogates this pathway. Here, we observed a paradoxical phenomenon. Immunoblot analysis revealed that neither CHD3 knockdown nor PARD3B overexpression caused a marked reduction in c-MYC protein levels in SWI/SNF-deficient cells (H23, H1703, TOV112D) **(**Fig. 4H–I**)**.

To resolve this paradox and identify upstream mechanisms driving MYC dysfunction, we performed WikiPathway analysis. Unlike GSEA, which captures broad trends in gene expression, WikiPathway analysis is based on curated signal transduction maps, enabling the identification of specific signaling cascades. We identified VEGFR2-associated pathways as common targets downregulated by CHD3 suppression/PARD3B overexpression and upregulated in SWI/SNF-deficient cells **(Supplementary Fig. 4M)**. VEGFR2 is known to regulate MYC via upstream PI3K-AKT and MAPK pathways. We therefore examined the phosphorylation status of major upstream effectors (VEGFR, AKT, ERK, STAT3). We found that while these pathways were partially suppressed in certain contexts, no specific kinase was uniformly inactivated across all cell lines upon CHD3 suppression or PARD3B overexpression **(Supplementary Fig. 4K–L, 4N–O)**. This heterogeneity suggests that PARD3B accumulation does not inhibit a single kinase but rather spatially perturbs signaling hubs, leading to context-dependent attenuation of upstream signals.

Collectively, these data lead us to conclude that PARD3B accumulation following CHD3 suppression causes a "functional uncoupling" of MYC—silencing its transcriptional output despite the presence of MYC protein—thereby triggering the collapse of pro-survival signaling.

**Therapeutic Exploitation of CHD3 Dependency in SWI/SNF-Deficient Cancers In Vivo**

Finally, we evaluated the therapeutic potential of targeting CHD3 *in vivo*. We established cell line-derived xenograft (CDX) models using SWI/SNF-deficient SBC-5 cells engineered to express doxycycline (Dox)-inducible Cas9 and single-guide RNAs (sgRNAs) targeting either a non-targeting control (sgNT) or *CHD3* (sgCHD3). In the control SBC-5-TRE-Cas9-sgNT xenograft model, Dox administration induced Cas9 expression but did not affect CHD3 protein levels, and no significant difference in tumor growth was observed compared to the vehicle-treated group **(**Figs. 5A–C**)**. Consistently, RT-qPCR analysis of tumor lysates confirmed that Dox treatment altered neither *CHD3* nor *PARD3B* mRNA expression levels **(**Fig. 5D**)**.

In stark contrast, Dox administration in the SBC-5-TRE-Cas9-sgCHD3 xenograft model induced potent tumor regression compared to controls **(**Figs. 5E and 5F**)**. Immunoblot analysis of tumor tissues confirmed the induction of Cas9 expression and the efficient depletion of CHD3 protein in Dox-treated tumors **(**Fig. 5G**)**. Furthermore, validating our *in vitro* findings, RT-qPCR analysis of residual tumor tissues revealed a significant downregulation of *CHD3* concomitant with a significant upregulation of *PARD3B* **(**Fig. 5H**)**. These results provide proof-of-concept that targeting CHD3 effectively exploits the epigenetic vulnerability of SWI/SNF-deficient cancers *in vivo*.

# Discussion

SWI/SNF-deficient cancers, particularly those characterized by the dual loss of SMARCA4 and SMARCA2, represent a therapeutic challenge due to their undifferentiated phenotype and lack of actionable drivers [2–5]. While current synthetic lethal strategies primarily exploit paralog dependencies—

such as targeting SMARCA2 in SMARCA4-deficient tumors [9–11] —our study uncovers a distinct vulnerability: a fatal "cross-complex dependency" on the CHD3/NuRD complex. We demonstrate that the loss of the SWI/SNF complex, a master regulator of chromatin accessibility [1], renders cancer cells strictly addicted to the opposing chromatin remodeler CHD3 to maintain epigenetic homeostasis. This finding expands the concept of synthetic lethality beyond gene families (paralogs) to inter-complex interactions, suggesting that the balance between distinct chromatin remodeling machineries is a critical determinant of cancer cell survival.

Recently, Schick et al. reported that the loss of SWI/SNF complex function is functionally compensated by another chromatin remodeler, the EP400/TIP60 complex [19]. Their study demonstrated that EP400 deficiency creates a synthetic lethal vulnerability to SWI/SNF inhibition, supporting the concept of functional interplay between distinct remodeling complexes. However, while their study highlighted that EP400 primarily maintains chromatin accessibility at gene promoters, our findings reveal that CHD3 plays a critical role predominantly at enhancer regions, such as the *PARD3B* enhancer. Indeed, in our screening, EP400 exhibited potent toxicity not only in SWI/SNF-deficient cells but also in proficient cells, limiting its selectivity as a therapeutic target in our context. In contrast, CHD3 inhibition demonstrated high selectivity for SWI/SNF-deficient cancers. This suggests that dependencies involving enhancer regulation (CHD3) may represent a more specific vulnerability in the context of SWI/SNF deficiency compared to those involving basal promoter functions (EP400).

A key conceptual advance of this study is the identification of "toxic derepression" as a driver of synthetic lethality. Unlike canonical synthetic lethal interactions that involve the loss of essential survival signals, we show that SWI/SNF-deficient cells succumb to death because they fail to repress a toxic gene, PARD3B, in the absence of CHD3. Our data indicate that CHD3, a core ATPase of the NuRD complex known to couple chromatin remodeling with histone deacetylation [20], functions as an essential "epigenetic brake" at the PARD3B enhancer. While NuRD complexes can function as transcriptional activators in certain contexts [21], our findings underscore its critical role as a repressor in this setting. In the absence of SWI/SNF-mediated regulation, this brake becomes the sole fail-safe mechanism; its removal triggers the unleashed expression of PARD3B to toxic levels. This gain-of-toxicity model provides a mechanistic rationale for why CHD3 is dispensable in normal cells but essential in the context of SWI/SNF deficiency.

Furthermore, we elucidate how PARD3B accumulation executes cell death by revealing a functional link to MYC signaling. Through GSEA analysis, we observed a paradoxical phenomenon where MYC target signatures were significantly suppressed despite stable c-MYC protein levels. We propose that this results from the "functional uncoupling" of MYC from its transcriptional output. PARD3B is a cell polarity regulator known to organize spatial signaling domains [18]. Its aberrant accumulation likely perturbs the spatial organization of upstream signaling hubs—such as PI3K/AKT and MAPK pathways—leading to a modest but global attenuation of kinase activities required for optimal MYC function. This spatial perturbation functionally dampens the MYC transcriptional program without triggering its degradation.

Given that SWI/SNF-deficient cancers are highly dependent on MYC signaling, the coordinate downregulation of the entire MYC network is sufficient to compromise cell survival, even in the absence of drastic silencing of individual target genes. Thus, the CHD3-PARD3B axis constitutes an epigenetic vulnerability that, when targeted, collapses the oncogenic MYC network upon which these cancers rely.

Clinically, our findings offer a promising therapeutic avenue for the most aggressive subset of SWI/SNF-deficient malignancies. Cancers with dual SMARCA4/SMARCA2 deficiency, including undifferentiated thoracic sarcomas [3] and a subset of lung adenocarcinomas [11], are refractory to emerging therapies that target SMARCA2 [9–11], as they lack the paralog target entirely. Our study positions CHD3 as a critical target specifically for this "treatment-refractory" population. Importantly, our *in vivo* analysis confirmed that tumor regression driven by CHD3 depletion was accompanied by the marked upregulation of *PARD3B*, mirroring the "toxic derepression" mechanism observed *in vitro*. By exploiting the cell's reliance on CHD3 to suppress PARD3B toxicity, CHD3-targeted therapy could induce tumor regression in patients who currently have no effective treatment options.

Regarding therapeutic modalities, our *in vivo* data demonstrate that depleting CHD3 protein using the CRISPR/Cas9 system is highly effective. Given that CHD3 functions as a structural component of the NuRD complex, simple enzymatic inhibition of its ATPase activity or associated HDAC activity might be insufficient to dislodge the complex from chromatin or release the epigenetic brake. Consistent with this, our screening revealed that the knockdown of HDAC1 and/or HDAC2 failed to induce synthetic lethality, and pharmacological HDAC inhibition using Vorinostat did not consistently induce PARD3B derepression. These findings strongly suggest that the structural integrity of the CHD3-containing complex, rather than its deacetylase activity alone, is critical for maintaining cell survival. Therefore, we propose that strategies inducing CHD3 protein degradation—such as Proteolysis Targeting Chimeras (PROTACs) [22] —represent the most viable approach for drug development.

Conceptually, our findings advocate for expanding the framework of synthetic lethality beyond the traditional "one-to-one" interaction model, where a single genetic alteration sensitizes cells to the inhibition of a single target. We propose that "next-generation" synthetic lethality involves higher-order relationships among three or more factors. Previously, we established a "one-to-two" synthetic lethal strategy, termed dual paralog inhibition, where a single genetic loss (e.g., SMARCB1 deficiency) creates a dependency on the simultaneous inhibition of two paralogous factors (e.g., CBP and p300) [12,13]. In contrast, the present study highlights a "two-to-one" model, where the dual deficiency of two genes (SMARCA4 and SMARCA2) converges to create a critical dependency on a single distinct factor (CHD3). These findings collectively suggest that cancer vulnerabilities are not limited to binary interactions but rather emerge from complex, multi-gene network imbalances. Therefore, future therapeutic strategies should focus on identifying and exploiting these "one-to-two" or "two-to-one" multi-factor relationships to broaden the scope of precision medicine for refractory cancers.

# Materials and Methods

# Animal ethics statement

All mouse experiments were approved by the National Cancer Center Animal Ethics Committee (Protocol Number: T19-013-M06) and were performed in accordance with the *Act on Welfare and Management of Animals* and the *Standards for Care and Keeping and Reducing Pain of Laboratory Animals*. Mice were monitored for clinical signs, tumor volume, and body weight as specified in the experimental protocols. Animals were euthanized before reaching the approved humane endpoints, defined as a tumor volume of 2,000 $mm^3$ or a body weight loss of 20% or the appearance of overt clinical signs of pain or distress. The maximum tumor burden was not exceeded in any of the experiments.

## Cell Lines and Culture Conditions

Cells were maintained at 37°C in a humidified incubator containing 5% $CO_2$. The culture medium comprised DMEM/F-12 (Wako, 048-29785) supplemented with 10% fetal bovine serum (FBS; Gibco/Life Technologies), 10% GlutaMAX Supplement (Gibco, 41550021), 100 U/mL penicillin, and 100 µg/mL streptomycin (Wako, 168-23191). Human lung cancer cell lines including NCI-H23 (RRID:CVCL_1547), NCI-H1703 (RRID:CVCL_1490), NCI-H2009 (RRID:CVCL_1514), NCI-H460 (RRID:CVCL_0459), NCI-H2228 (RRID:CVCL_1543), NCI-H358 (RRID:CVCL_1559), NCI-H1048 (RRID:CVCL_1453), PC-9 (RRID:CVCL_B260), DMS-114 (RRID:CVCL_1174), SBC-5 (RRID:CVCL_1679), A549 (RRID:CVCL_0023), NCI-H1299 (RRID:CVCL_0060), NCI-H1819 (RRID:CVCL_1497), and NCI-H661 (RRID:CVCL_1577), and ovarian cancer cell lines including TOV-112D (RRID:CVCL_3612), ES-2 (RRID:CVCL_3509), and RMG-I (RRID:CVCL_1662) were used in this study. NCI-H23, NCI-H1703, NCI-H2009, NCI-H460, NCI-H2228, NCI-H358, NCI-H1048, DMS-114, A549, NCI-H1299, NCI-H1819, NCI-H661, TOV-112D, and ES-2 were obtained from the American Type Culture Collection (ATCC). PC-9 was obtained from Immuno-Biological Laboratories (IBL). SBC-5 and RMG-I were obtained from the Japanese Collection of Research Bioresources (JCRB) Cell Bank. All cell lines except for NCI-H2009, NCI-H1048, SBC-5 and RMG-I were authenticated by sequencing and comparing short tandem repeats (STRs) (Promega Corporation) and tested negative for Mycoplasma using MycoAlert (Lonza, LT07-318). All cell lines were used for functional experiments within 2 months of passage post-receipt.

## Generation of Lentiviruses and Viral Transduction

To generate lentiviral particles, 293LTV cells were transfected with lentiviral plasmids and packaging plasmids using Lipofectamine 3000 (Thermo Fisher Scientific; L3000015). After 16 hours, the medium was replaced with fresh growth medium, and cells were incubated for an additional 48 hours. Lentivirus-containing supernatants were harvested and concentrated by centrifugation using Lenti-X Concentrator (Takara; 631232). To establish the H23 isogenic model, SMARCA4-deficient H23 cells were transduced with lentiviral particles carrying human *SMARCA4* (pLV[Exp]-Puro-CMV>hSMARCA4[NM_001128849.1]; Vector Builder, VB181029-1161teb) in the presence of 8 µg/mL polybrene (Nacalai Tesque; 12996-81). After 24 h of incubation, the medium was replaced with fresh growth medium. Between 24 and 48 h

post-transduction, cells were subjected to selection in growth medium containing 2 μg/mL puromycin (Wako; 160-23151) for 3–7 days. For PARD3B overexpression, cells were transduced with lentiviral particles encoding full-length *PARD3B* cDNA (Precision LentiORF PARD3B; Dharmacon, PLOHS_100061657, OHS5898-202623935). Cells were harvested 96 h post-transduction for immunoblotting or RNA extraction for RNA-seq analysis.

# siRNA Screening, Cell Viability, and Colony Formation Assays

For the chromatin remodeling factor screen, a custom siRNA library targeting 17 ATP-dependent chromatin remodeling factors (excluding SWI/SNF subunits) and NuRD complex components was synthesized by Dharmacon. To ensure robust gene silencing, a double transfection protocol was employed. Briefly, SWI/SNF-deficient H23 cells and SMARCA4-restored cells were seeded in 24-well plates at a density of $2 \times 10^5$ cells per well and transfected with siRNAs (final concentration 20 nM) using Lipofectamine RNAiMAX (Thermo Fisher Scientific; 13778150) according to the manufacturer's instructions. Forty-eight hours post-transfection, cells were trypsinized, reseeded in 24-well plates, and subjected to a second round of transfection with siRNAs (20 nM). After an additional 48 hours, cells were trypsinized, counted, and re-plated into 96-well plates at a density of 500 cells per well. Cell viability was assessed 7 days after the final plating by measuring cellular ATP levels using the CellTiter-Glo Luminescent Cell Viability Assay (Promega; G7571). For colony formation assays, 1,000 cells were seeded in 6-well plates, treated as indicated, and cultured for 10–14 days. Colonies were fixed with methanol and stained with 0.5% crystal violet solution. The ON-TARGETplus SMARTpool siRNAs targeting CHD3 (L-023015-00), PARD3B (L-017697-02), and Non-targeting control (D-001810-10) were purchased from Dharmacon. A complete list of siRNAs used in the screen is provided in **Supplementary Table 1**.

# Immunoblot Analysis

To extract proteins, $5 \times 10^5$ cells were harvested, washed with PBS, and lysed with 150 μL of 1 × SDS sample buffer at 95°C for 5 min. Chromatin was sonicated on ice (20 cycles of 15-second pulses; high setting; 15 seconds between pulses) using a Bioruptor (M&S Instruments). The cell lysates were quantified using Pierce 660nm Protein Assay Reagent (Thermo Fisher Scientific, 22660) and Ionic Detergent Compatibility Reagent for Pierce™ 660nm Protein Assay Reagent (Thermo Fisher Scientific, 22663). Next, 15 μg of protein was analyzed by immunoblotting. SDS-PAGE separated proteins, transferred them to PVDF membranes, and immunoblotted with the indicated antibodies. β-actin was used as a loading control. Membranes were blocked for 1 hour at 25°C with PVDF Blocking Reagent for Can Get Signal (TOYOBO, NYPBR01) and then probed for 1 hour at 25°C with Can Get Signal Solution 1 (TOYOBO, NKB-201) containing primary antibodies. After washing with TBS containing 0.1% Tween 20, the membranes were incubated for 30 min at 25°C with TBS containing 0.1% Tween 20, 1% BSA, and horseradish peroxidase-conjugated anti-mouse (CST, 7076) (RRID: AB_330924) or anti-rabbit (CST, 7074) (RRID: AB_2099233) secondary antibodies before visualization using Western Lightning ECL Pro (Perkin

Elmer, NEL120001EA). Chemiluminescence signals were measured using a FUSION Chemiluminescence Imaging System (M&S Instruments). Antibodies specific to the proteins were used for immunoblotting, as provided in **Supplementary Table 2**.

# GFP-based Competition Assay

To evaluate the long-term effect of CHD3 depletion on cell proliferation, we performed a GFP-based competition assay using the SMARTvector Inducible Lentiviral shRNA system (Horizon Discovery). SWI/SNF-deficient (H23) and -proficient (H460) cells were transduced with lentiviral vectors encoding a Doxycycline (Dox)-inducible shRNA targeting CHD3 (Catalog #V3IHSMCG_6422690) or a Non-targeting control (Catalog #VSC11651). In this system, the expression of both the shRNA and the TurboGFP reporter is driven by the Tet-inducible promoter. Stable cell lines were established by Puromycin selection. For the competition assay, shRNA-transduced cells were mixed with parental isogenic cells at a 1:1 ratio. The mixed populations were cultured in the presence of Dox (1 μg/mL) to induce the expression of shRNA and TurboGFP. Cells were passaged every 2–3 days, at which time the culture medium containing Dox was refreshed to maintain induction. The percentage of TurboGFP-positive cells was monitored at the indicated time points using a Guava flow cytometer (Millipore). Relative cell viability was calculated by dividing the percentage of TurboGFP-positive cells at each indicated time point by the percentage of TurboGFP-positive cells at Day 0, and expressed as a percentage relative to the initial time point. A decrease in the relative viability indicates a proliferation defect or cell death induced by the shRNA.

# Quantitation of mRNA

To measure basal mRNA levels, $2 \times 10^4$ cells were plated into 96-well plates and incubated for 24 h. For siRNA knockdown experiments, $2 \times 10^4$ cells were plated into 96-well plates and transfected with siRNAs (20 nM) using Lipofectamine RNAiMAX (Thermo Fisher Scientific; 13778150). Cells were harvested after 48–96 h of incubation. For drug-treated cells, $2 \times 10^4$ cells were plated into 96-well plates and incubated for 24 h. The medium was then replaced with a medium containing Vorinostat (Selleck, S1047) and incubated for 24 hours. Cell lysis and cDNA synthesis were performed using the SuperPrep II Cell Lysis & RT Kit for qPCR (TOYOBO; SCQ-401) according to the manufacturer's instructions. Quantitative PCR was performed using the THUNDERBIRD Probe qPCR Mix (TOYOBO; QPS101) and TaqMan Gene Expression Assays (Thermo Fisher Scientific). For the extraction of mRNA from tumor samples, the tumor xenograft samples were harvested, weighed, and washed with PBS. Tissue samples (approximately 30 mg) were pulverized in liquid nitrogen and processed using the RNeasy Mini Kit (QIAGEN; 74104) in conjunction with QIAshredder columns (QIAGEN; 79654), according to the manufacturer’s protocol for animal tissues. RNA was eluted in a final volume of 50 μL. Subsequently, cDNA was synthesized using PrimeScript RT Master Mix (Perfect Real Time) (Takara Bio; RR036A). The following gene-specific primer/probe sets were used: *CHD3* (Hs01050212_m1), *PARD3B* (Hs01565182_m1), and *GAPDH* (Hs99999905_m1). PCR was performed on an ABI StepOnePlus Real-Time PCR System (Applied Biosystems; RRID:SCR_015805) under the following conditions: denaturation at 95°C for 15 seconds, followed by annealing and extension at 60°C for 30 seconds (40 cycles). Relative mRNA expression

levels were calculated using the comparative Ct ($2^{-\Delta\Delta Ct}$) method, with *GAPDH* serving as the internal control.

# RNA-seq analysis

To measure basal mRNA levels or assess gene expression changes upon genetic manipulation, $4 \times 10^5$ cells were plated into 6-well plates for 24 h. For knockdown experiments, cells were transfected with siRNAs (20 nM) using Lipofectamine RNAiMAX (Thermo Fisher Scientific; 13778150) and harvested after 96 h of incubation. For overexpression experiments, cells were transduced with lentiviral cDNA expression vectors and harvested after 96 h. Total RNA was isolated using the RNeasy Mini Kit (Qiagen; 74104) according to the manufacturer's instructions. Library preparation and sequencing were performed by Rhelixa, Inc. (Tokyo, Japan). mRNA was purified using the Poly(A) mRNA Magnetic Isolation Module (New England Biolabs), and libraries were constructed using the NEBNext Ultra II Directional RNA Library Prep Kit for Illumina (New England Biolabs). Sequencing was performed on an Illumina NovaSeq 6000 platform (150 bp paired-end reads).

# ATAC-seq analysis

To assess proliferating cells, cells ($2 \times 10^5$) were plated on a 12-well plate and incubated for 24 h. For knockdown experiments, cells ($2 \times 10^5$) were cultured in 12-well plates and transfected with siRNAs (20 nM) using Lipofectamine RNAiMAX (Thermo Fisher Scientific; 13778150). After 96 h of incubation, cells were harvested. ATAC-seq library preparation and sequencing were performed by DNAFORM (Yokohama, Japan). Briefly, $1 \times 10^5$ viable cells were lysed, and the transposition reaction was performed using Tn5 Transposase (Illumina; FC-121-1030) at 37°C for 30 min. The transposed DNA was purified using the MinElute PCR Purification Kit (Qiagen; 28004). Library amplification was performed using NEBNext Q5 Hot Start HiFi PCR Master Mix (New England Biolabs; M0543S) and custom Nextera PCR primers [23]. Five cycles of initial PCR were conducted, and the number of additional cycles was determined by quantitative PCR (qPCR) analysis of the partially amplified products. The final libraries were purified using Agencourt AMPure XP beads (Beckman Coulter; A63881) with double size selection (ratios: 0.5× and 1.4×) according to the manufacturer’s protocol. Sequencing was performed on an MGI Tech DNBSEQ-G400R platform (150 bp paired-end reads). Data processing, including read mapping and peak calling, was performed using the ENCODE ATAC-seq pipeline (https://github.com/ENCODE-DCC/atac-seq-pipeline). Reads were mapped to the human reference genome (hg38) using Bowtie2 (v2.3.4.3) [24], and duplicate reads were removed using Picard (v2.20.7) and samtools (v1.9). Peak calling was performed using MACS2 (v2.2.4) with default parameters. After the removal of blacklisted regions, peak consistency between replicates was assessed using the Irreproducible Discovery Rate (IDR) framework (v2.0.4.2). Peak annotation was performed using HOMER (v4.9.1) with default settings. Differentially accessible peaks were identified using DESeq2 (v1.20.0).

# CUT&RUN-seq analysis

To assess proliferating cells, $5 \times 10^5$ cells were seeded in 6-well plates and incubated for 24 hours. CUT&RUN analysis was performed using the CUT&RUN Assay Kit (Cell Signaling Technology [CST]; 86652). Cells were harvested by trypsinization, and $5 \times 10^5$ cells were suspended in 1× Wash Buffer and bound to concanavalin A-coated beads. Cells were permeabilized with 100 µL of Antibody Binding Buffer containing digitonin and incubated at 4°C for 2 h with 2 µL of the following primary antibodies: anti-H3K4me3 (CST, 9751; RRID:AB_2616028), anti-H3K4me1 (CST, 5326; RRID:AB_10695860), anti-H3K27ac (CST, 8173; RRID:AB_2616015), anti-H3K27me3 (CST, 9733; RRID:AB_2616029), anti-SMARCA4 (Abcam, ab110641; RRID:AB_10860265), anti-CHD3 (Bethyl Laboratories, A301-219A; RRID:AB_890566). Cells were washed four times with Digitonin Buffer, incubated with pAG-MNase solution at 4°C for 1 h, and washed an additional four times. MNase was activated by adding 3 µL of $CaCl_2$ solution at 4°C for 30 min, and the reaction was stopped by adding 1 × Stop Buffer. For input DNA preparation, $1 \times 10^5$ cells were treated with DNA Extraction Buffer containing RNase and Proteinase K, followed by incubation at 55°C for 1 hour. The genomic DNA was sonicated to yield fragments of 150–500 bp (40 cycles of 15 sec on/30 sec off, high setting) using a Bioruptor (M&S Instruments). Chromatin and input DNA were purified using DNA Purification Buffers and Spin Columns (CST; 14209). Libraries were constructed using the ThruPLEX DNA-Seq Kit (Takara; R400674) and amplified for 16 cycles (denaturation at 98°C for 20 sec; annealing and extension at 72°C for 50 sec). Sequencing was performed by Takara Bio using the Illumina NovaSeq 6000 platform (150 bp paired-end reads).

# Unified Data Processing Pipeline

**Data Preprocessing and RNA-seq Analysis**: Raw sequencing reads from all applications were trimmed using fastp (version 0.12.4; RRID:SCR_016962) [25]. For RNA-seq data, trimmed reads were mapped to the human reference genome (hg38) using HISAT2 (version 2.2.1; RRID:SCR_015530) [26]. Gene expression levels were quantified as Transcripts Per Million (TPM) using Strand NGS (version 4.0; TOMY Digital Biology). Differential expression analysis was performed using Strand NGS, identifying differentially expressed genes (DEGs) based on the criteria of $P < 0.05$ and $|\log2(\text{Fold Change})| > 1$. Venn diagram generation and WikiPathway analysis were subsequently performed on these DEG lists using Strand NGS.

**ATAC-seq and CUT&RUN Data Processing**: For ATAC-seq and CUT&RUN data, trimmed reads were mapped to hg38 using Bowtie2 (version 2.4.5; RRID:SCR_016368) [24] with the following parameters: -k 1 --no-mixed --no-discordant -X 2000. PCR duplicates were removed using the MarkDuplicates command in Picard (version 2.26.11; RRID:SCR_006525) [http://broadinstitute.github.io/picard].

**Visualization and Genome Browser Tracks**: Genome browser tracks (BigWig files) were generated using deepTools (version 3.5.1; RRID:SCR_016366) [27]. For ATAC-seq and RNA-seq data, the bamCoverage command was used with the following parameters: --normalizeUsing CPM --binSize 10 --smoothLength 30. For CUT&RUN data, background signals were subtracted using input controls. The bamCompare command was used with the following parameters: --operation subtract --normalizeUsing CPM --

scaleFactorsMethod None --binSize 10 --smoothLength 30. The resulting BigWig files were visualized using the Integrative Genomics Viewer (IGV) (version 2.13.2; RRID:SCR_011793) [28].

**Genomic Signal Distribution Analysis**

To visualize the genome-wide distribution of CUT&RUN signals relative to transcription start sites (TSS), we utilized the deepTools suite. Read coverage scores were calculated using the computeMatrix reference-point module. The analysis window was defined as 3 kb upstream and 3 kb downstream of the TSS, based on the GENCODE v38 annotation (hg38). Heatmaps were generated using the plotHeatmap module with k-means clustering (k = 3) to classify regions based on signal enrichment patterns.

# Gene Set Enrichment Analysis (GSEA) (Final Draft)

Read counts were generated using FeatureCounts (version 2.0.6) [29]. Gene Set Enrichment Analysis (GSEA) was performed using the GSEA software (version 4.3.2) [30] in conjunction with the Molecular Signatures Database (MSigDB) [30]. Specifically, the hallmark gene sets were utilized to identify significantly enriched biological pathways. Gene sets were considered statistically significant if they met the criteria of a False Discovery Rate (FDR) *q*-value < 0.25 and a nominal *P*-value < 0.05.

# Mouse xenograft model

In the doxycycline (Dox) treatment study, cells were counted and resuspended in a 1:1 mixture of PBS and Matrigel (Corning; 354234) on ice. SBC-5 cells ($5 \times 10^5$ cells per mouse) were injected subcutaneously into the flank of 5–6-week-old female BALB/*c-nu/nu* mice (CLEA Japan). The total injection volume was 200 µL. When tumors became palpable (approximately 14 to 21 days post-implantation), mice were randomized into two groups and fed either a diet containing Dox (625 ppm; Research Diets, D13110903) or a control diet (Research Diets; D10001). Tumor growth was monitored twice weekly using calipers. Tumor volume was calculated using the formula $V = (L \times W^2)/2$, where V is volume ($mm^3$), L is the largest diameter (mm), and W is the smallest diameter (mm). At the experimental endpoint, mice were euthanized in accordance with institutional guidelines and standard protocols.

# Data availability statement

All raw NGS data files (RNA-seq, ATAC-seq, and CUT&RUN-seq) and processed bigWig files have been deposited in the NCBI Gene Expression Omnibus (GEO) under the accession number [GSE].

# Statistical Analysis

Data were analyzed using GraphPad Prism software (version [10.4.1]; GraphPad Software). Statistical significance was determined using two-tailed Student's *t*-test for two-group comparisons. A *P*-value < 0.05 was considered statistically significant.

## Declarations

# Author Disclosures

H.O. received research grants from Ono Pharmaceutical Co., Ltd. during the conduct of the study. The other authors declare no competing interests.

**Competing Interests**

H.O. received research grants from Ono Pharmaceutical Co., Ltd. during the conduct of the study. The other authors declare no competing interests.

# Author Contribution

Conceptualization: H.O.; Data curation: M.T., Y.O., M.F., H.H., H.O.; Formal analysis: M.T., Y.O., M.F., H.H., H.O.; Funding acquisition: H.O.; Investigation: M.T., Y.O., M.F., H.H., H.O.; Methodology: M.T., H.O.; Project administration: M.T., H.O.; Resources: M.T., Y.O., M.F., H.H., H.O.; Supervision: H.O.; Validation: M.T., Y.O., M.F., H.H., H.O.; Visualization: M.T., H.O.; Writing – original draft: M.T., H.O.; Writing – review & editing: M.T., Y.O., M.F., H.H., H.O.

# Acknowledgement

We thank Rie Komatsuzaki, Keiko Nakasato, and Hinako Masuda for their technical assistance, and we also appreciate the support of Yoshinori Ishikawa and Ryohei Kozaki for this project. This study was supported by the Japan Agency for Medical Research and Development (AMED) (Grant JP21cm0106185 to H.O.), the Kobayashi Foundation for Cancer Research (Grant 2020 to H.O.), and Ono Pharmaceutical Co., Ltd. (Grant C2022-129 to H.O.).

# Data Availability

All raw NGS data files (RNA-seq, ATAC-seq, and CUT&RUN-seq) and processed bigWig files have been deposited in the NCBI Gene Expression Omnibus (GEO) under the accession number [GSE].

## References

1. Kadoch, C., Hargreaves, D.C., Hodges, C., Elias, L., Ho, L., Ranish, J., and Crabtree, G.R. (2013). Proteomic and bioinformatic analysis of mammalian SWI/SNF complexes identifies extensive roles in human malignancy. Nat Genet *45*, 592–601. 10.1038/ng.2628.
2. Witkowski, L., Carrot-Zhang, J., Albrecht, S., Fahiminiya, S., Hamel, N., Tomiak, E., Grynspan, D., Saloustros, E., Nadaf, J., Rivera, B., et al. (2014). Germline and somatic SMARCA4 mutations characterize small cell carcinoma of the ovary, hypercalcemic type. Nat Genet *46*, 438–443. 10.1038/ng.2931.

3. Le Loarer, F., Watson, S., Pierron, G., de Montpreville, V.T., Ballet, S., Firmin, N., Auguste, A., Pissaloux, D., Boyault, S., Paindavoine, S., et al. (2015). SMARCA4 inactivation defines a group of undifferentiated thoracic malignancies transcriptionally related to BAF-deficient sarcomas. Nat Genet *47*, 1200–1205. 10.1038/ng.3399.
4. Schoenfeld, A.J., Bandlamudi, C., Lavery, J.A., Montecalvo, J., Namakydoust, A., Rizvi, H., Egger, J., Concepcion, C.P., Paul, S., Arcila, M.E., et al. (2020). The Genomic Landscape of SMARCA4 Alterations and Associations with Outcomes in Patients with Lung Cancer. Clin Cancer Res *26*, 5701–5708. 10.1158/1078 – 0432.CCR-20-1825.
5. Karnezis, A.N., Wang, Y., Ramos, P., Hendricks, W.P., Oliva, E., D'Angelo, E., Prat, J., Nucci, M.R., Nielsen, T.O., Chow, C., et al. (2016). Dual loss of the SWI/SNF complex ATPases SMARCA4/BRG1 and SMARCA2/BRM is highly sensitive and specific for small cell carcinoma of the ovary, hypercalcaemic type. J Pathol *238*, 389–400. 10.1002/path.4633.
6. Mittal, P., and Roberts, C.W.M. (2020). The SWI/SNF complex in cancer - biology, biomarkers and therapy. Nat Rev Clin Oncol *17*, 435–448. 10.1038/s41571-020-0357-3.
7. Wilson, B.G., Wang, X., Shen, X., McKenna, E.S., Lemieux, M.E., Cho, Y.J., Koellhoffer, E.C., Pomeroy, S.L., Orkin, S.H., and Roberts, C.W. (2010). Epigenetic antagonism between polycomb and SWI/SNF complexes during oncogenic transformation. Cancer Cell *18*, 316–328. 10.1016/j.ccr.2010.09.006.
8. Bitler, B.G., Aird, K.M., Garipov, A., Li, H., Amatangelo, M., Kossenkov, A.V., Schultz, D.C., Liu, Q., Shih Ie, M., Conejo-Garcia, J.R., et al. (2015). Synthetic lethality by targeting EZH2 methyltransferase activity in ARID1A-mutated cancers. Nat Med *21*, 231–238. 10.1038/nm.3799.
9. Hoffman, G.R., Rahal, R., Buxton, F., Xiang, K., McAllister, G., Frias, E., Bagdasarian, L., Huber, J., Lindeman, A., Chen, D., et al. (2014). Functional epigenetics approach identifies BRM/SMARCA2 as a critical synthetic lethal target in BRG1-deficient cancers. Proc Natl Acad Sci U S A *111*, 3128–3133. 10.1073/pnas.1316793111.
10. Wilson, B.G., Helming, K.C., Wang, X., Kim, Y., Vazquez, F., Jagani, Z., Hahn, W.C., and Roberts, C.W. (2014). Residual complexes containing SMARCA2 (BRM) underlie the oncogenic drive of SMARCA4 (BRG1) mutation. Mol Cell Biol *34*, 1136–1144. 10.1128/MCB.01372-13.
11. Oike, T., Ogiwara, H., Tominaga, Y., Ito, K., Ando, O., Tsuta, K., Mizukami, T., Shimada, Y., Isomura, H., Komachi, M., et al. (2013). A synthetic lethality-based strategy to treat cancers harboring a genetic deficiency in the chromatin remodeling factor BRG1. Cancer Res *73*, 5508–5518. 10.1158/0008-5472.CAN-12-4593.
12. Sasaki, M., Kato, D., Murakami, K., Yoshida, H., Takase, S., Otsubo, T., and Ogiwara, H. (2024). Targeting dependency on a paralog pair of CBP/p300 against de-repression of KREMEN2 in SMARCB1-deficient cancers. Nat Commun *15*, 4770. 10.1038/s41467-024-49063-w.
13. Sasaki, M., Kato, D., Yoshida, H., Shimizu, T., and Ogiwara, H. (2025). Efficacy of CBP/p300 Dual Inhibitors against Derepression of KREMEN2 in cBAF-Deficient Cancers. Cancer Res Commun *5*, 24–38. 10.1158/2767–9764.CRC-24-0484.

14. Clapier, C.R., Iwasa, J., Cairns, B.R., and Peterson, C.L. (2017). Mechanisms of action and regulation of ATP-dependent chromatin-remodelling complexes. Nat Rev Mol Cell Biol *18*, 407–422. 10.1038/nrm.2017.26.
15. Tong, J.K., Hassig, C.A., Schnitzler, G.R., Kingston, R.E., and Schreiber, S.L. (1998). Chromatin deacetylation by an ATP-dependent nucleosome remodelling complex. Nature *395*, 917–921. 10.1038/27699.
16. Xue, Y., Wong, J., Moreno, G.T., Young, M.K., Cote, J., and Wang, W. (1998). NURD, a novel complex with both ATP-dependent chromatin-remodeling and histone deacetylase activities. Mol Cell *2*, 851–861. 10.1016/s1097-2765(00)80299-3.
17. Bornelov, S., Reynolds, N., Xenophontos, M., Gharbi, S., Johnstone, E., Floyd, R., Ralser, M., Signolet, J., Loos, R., Dietmann, S., et al. (2018). The Nucleosome Remodeling and Deacetylation Complex Modulates Chromatin Structure at Sites of Active Transcription to Fine-Tune Gene Expression. Mol Cell *71*, 56–72 e54. 10.1016/j.molcel.2018.06.003.
18. Thompson, B.J. (2022). Par-3 family proteins in cell polarity & adhesion. FEBS J *289*, 596–613. 10.1111/febs.15754.
19. Martin, B.J.E., Ablondi, E.F., Goglia, C., Mimoso, C.A., Espinel-Cabrera, P.R., and Adelman, K. (2023). Global identification of SWI/SNF targets reveals compensation by EP400. Cell *186*, 5290–5307 e5226. 10.1016/j.cell.2023.10.006.
20. Denslow, S.A., and Wade, P.A. (2007). The human Mi-2/NuRD complex and gene regulation. Oncogene *26*, 5433–5438. 10.1038/sj.onc.1210611.
21. Hoffmeister, H., Fuchs, A., Erdel, F., Pinz, S., Grobner-Ferreira, R., Bruckmann, A., Deutzmann, R., Schwartz, U., Maldonado, R., Huber, C., et al. (2017). CHD3 and CHD4 form distinct NuRD complexes with different yet overlapping functionality. Nucleic Acids Res *45*, 10534–10554. 10.1093/nar/gkx711.
22. Farnaby, W., Koegl, M., Roy, M.J., Whitworth, C., Diers, E., Trainor, N., Zollman, D., Steurer, S., Karolyi-Oezguer, J., Riedmueller, C., et al. (2019). Publisher Correction: BAF complex vulnerabilities in cancer demonstrated via structure-based PROTAC design. Nat Chem Biol *15*, 846. 10.1038/s41589-019-0329-z.
23. Buenrostro, J.D., Giresi, P.G., Zaba, L.C., Chang, H.Y., and Greenleaf, W.J. (2013). Transposition of native chromatin for fast and sensitive epigenomic profiling of open chromatin, DNA-binding proteins and nucleosome position. Nat Methods *10*, 1213–1218. 10.1038/nmeth.2688.
24. Langmead, B., and Salzberg, S.L. (2012). Fast gapped-read alignment with Bowtie 2. Nat Methods *9*, 357–359. 10.1038/nmeth.1923.
25. Chen, S., Zhou, Y., Chen, Y., and Gu, J. (2018). fastp: an ultra-fast all-in-one FASTQ preprocessor. Bioinformatics *34*, i884-i890. 10.1093/bioinformatics/bty560.
26. Kim, D., Paggi, J.M., Park, C., Bennett, C., and Salzberg, S.L. (2019). Graph-based genome alignment and genotyping with HISAT2 and HISAT-genotype. Nat Biotechnol *37*, 907–915. 10.1038/s41587-019-0201-4.

27. Ramirez, F., Dundar, F., Diehl, S., Gruning, B.A., and Manke, T. (2014). deepTools: a flexible platform for exploring deep-sequencing data. Nucleic Acids Res *42*, W187-191. 10.1093/nar/gku365.

28. Robinson, J.T., Thorvaldsdottir, H., Winckler, W., Guttman, M., Lander, E.S., Getz, G., and Mesirov, J.P. (2011). Integrative genomics viewer. Nat Biotechnol *29*, 24–26. 10.1038/nbt.1754.

29. Liao, Y., Smyth, G.K., and Shi, W. (2014). featureCounts: an efficient general purpose program for assigning sequence reads to genomic features. Bioinformatics *30*, 923–930. 10.1093/bioinformatics/btt656.

30. Subramanian, A., Tamayo, P., Mootha, V.K., Mukherjee, S., Ebert, B.L., Gillette, M.A., Paulovich, A., Pomeroy, S.L., Golub, T.R., Lander, E.S., and Mesirov, J.P. (2005). Gene set enrichment analysis: a knowledge-based approach for interpreting genome-wide expression profiles. Proc Natl Acad Sci U S A *102*, 15545–15550. 10.1073/pnas.0506580102.

# Figures

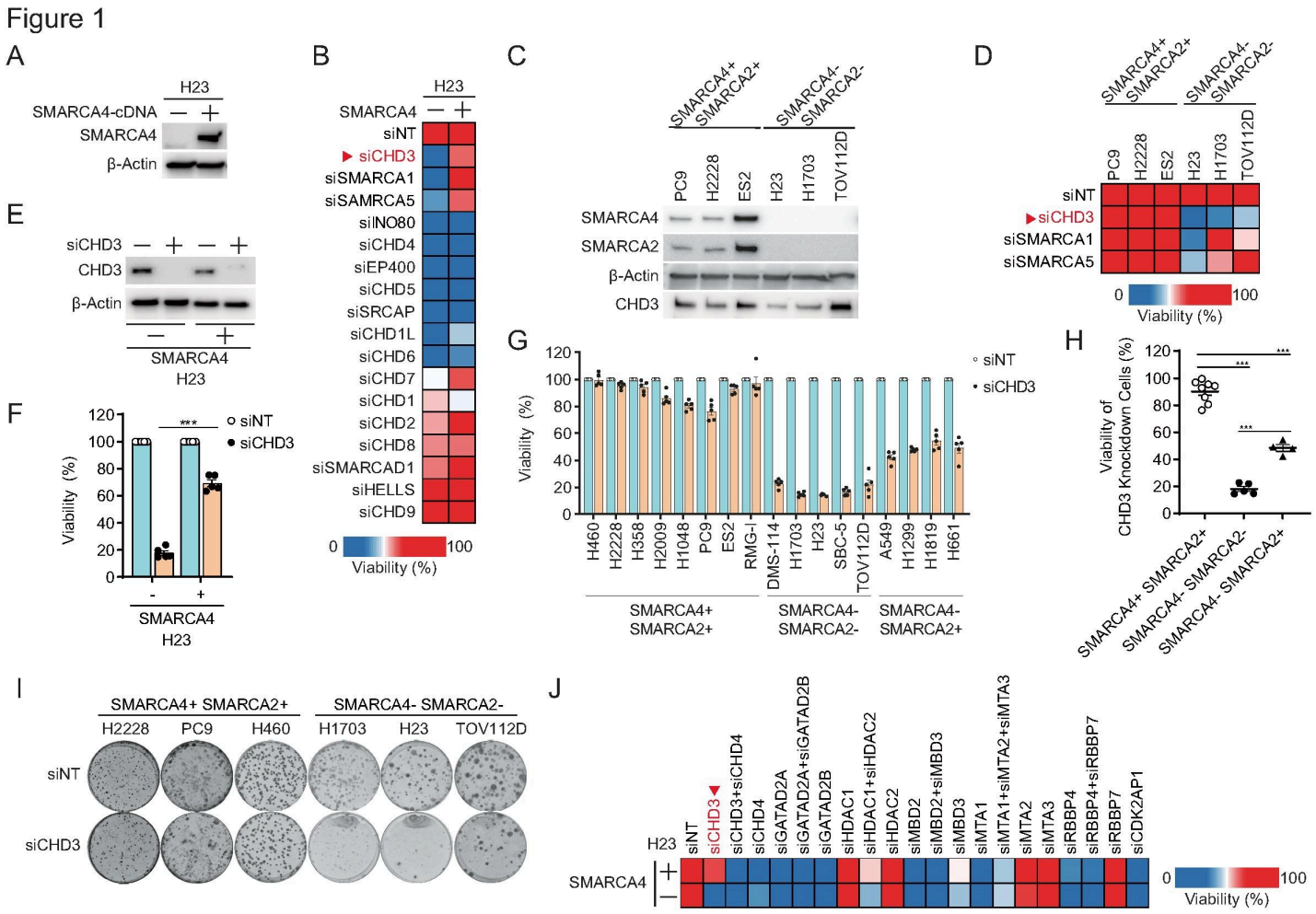



**Figure 1**

**Identification of CHD3 as a Specific Synthetic Lethal Target in SWI/SNF-Deficient Cancers**

**(A)** Immunoblot analysis of SMARCA4 expression in the isogenic model established from SMARCA4/SMARCA2-deficient H23 lung cancer cells and SMARCA4-cDNA restored H23 cells. β-Actin served as a loading control.

**(B)** Heatmap showing the results of an siRNA screen targeting 17 ATP-dependent chromatin remodeling factors (excluding SWI/SNF subunits) in H23 cells. Blue indicates reduced cell viability. CHD3, SMARCA1, and SMARCA5 were identified as top candidates.

**(C)** Immunoblot characterization of a cell line panel comprising SWI/SNF-proficient (SMARCA4+/SMARCA2+) and SWI/SNF-dual-deficient (SMARCA4-/SMARCA2-) lung and ovarian cancer lines.

**(D)** Heatmap depicting the relative viability of SWI/SNF-proficient and -deficient cell lines treated with siRNAs targeting the candidates identified in **(B)**. Note that *CHD3* depletion selectively impacts SWI/SNF-deficient lines, whereas *SMARCA1* and *SMARCA5*depletion exhibit general toxicity.

**(E)** Immunoblot validation of CHD3 knockdown efficiency in the H23 isogenic pair treated with control (siNT) or *CHD3*-targeting siRNA (siCHD3).

**(F)** Cell viability of the H23 isogenic pair following *CHD3* knockdown. Data are normalized to siNT.

**(G)** Cell viability profile of the expanded cell line panel following *CHD3* knockdown. Cells are grouped by SWI/SNF mutation status.

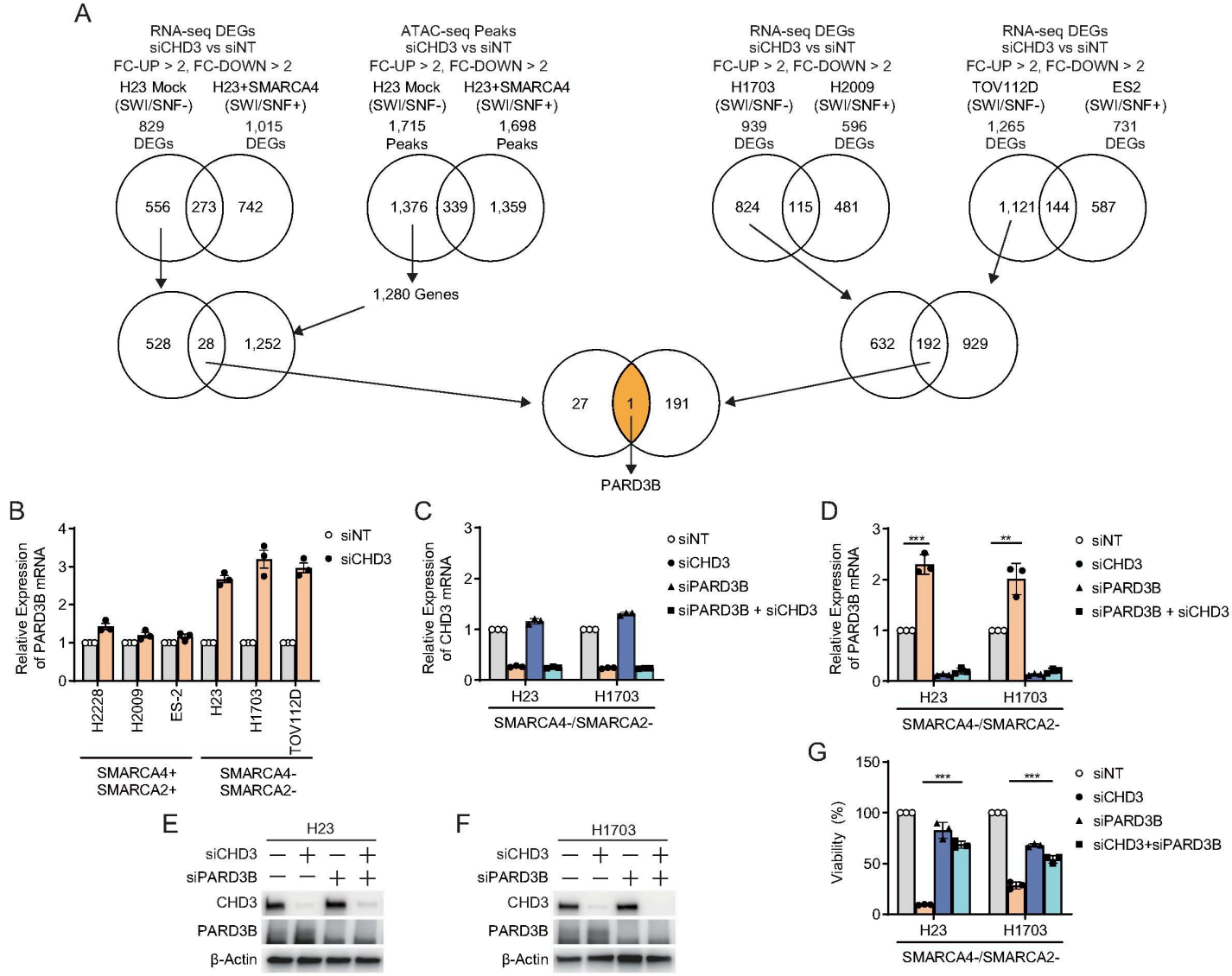
**(H)** Dot plot summarizing the viability of CHD3-depleted cells from **(G)**. Note that dual-deficient cells (SMARCA4-/SMARCA2-) show significantly higher sensitivity compared to proficient and single-deficient cells.

**(I)** Representative crystal violet staining images of the cell line panel treated with siNT or siCHD3.

**(J)** Heatmap showing the relative viability of H23 cells following knockdown of individual NuRD complex subunits.

Data are presented as mean ± SD. *P < 0.05, **P < 0.01, ***P < 0.001 (Student's t-test). **See also Figure S1.**

Figure 2




## Figure 2

### Toxic Overexpression of PARD3B Drives CHD3 Synthetic Lethality

**(A)** Integrated identification of synthetic lethal mediators. **(Left)** Venn diagrams summarizing the number of differentially expressed genes (RNA-seq) and altered chromatin peaks (ATAC-seq) in the H23 isogenic model upon *CHD3* knockdown. Genes and peaks specifically altered in SWI/SNF-deficient H23 Mock cells were intersected. **(Right)**RNA-seq analysis of lung (H1703 vs H2009) and ovarian (TOV112D vs ES-2) cancer cell lines. Overlap analysis identified *PARD3B* as the sole common candidate gene upregulated specifically in SWI/SNF-deficient cells upon *CHD3*depletion.

**(B)** RT-qPCR analysis of *PARD3B* mRNA levels in SWI/SNF-proficient and -deficient cell lines treated for 48 h with control (siNT) or *CHD3*-targeting siRNA (siCHD3). Note the robust induction of *PARD3B* specifically in deficient lines.

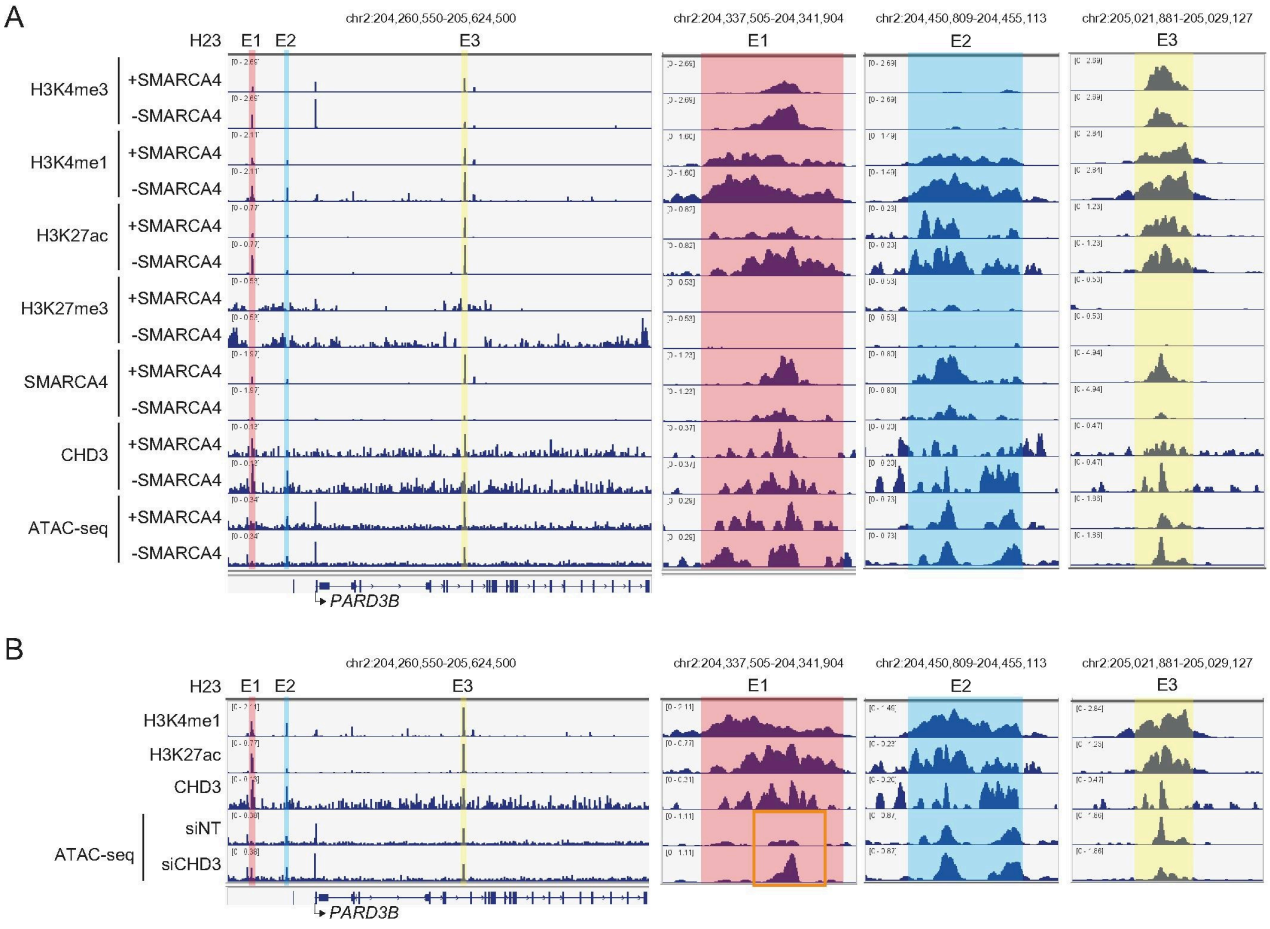
**(C, D)** RT-qPCR analysis of *CHD3* **(C)**and *PARD3B* **(D)** mRNA levels in SWI/SNF-deficient lung cancer cell lines (H23, H1703) treated for 48 h with siNT, siCHD3, *PARD3B*-targeting siRNA (siPARD3B), or the combination (siCHD3+siPARD3B).

**(E, F)** Immunoblot analysis of CHD3 and PARD3B proteins in H23 **(E)** and H1703 **(F)** cells treated as indicated. β-Actin served as a loading control.

**(G)** Cell viability of H23 and H1703 cells treated as indicated. Simultaneous knockdown of *PARD3B* significantly rescues the lethality induced by *CHD3* loss.

Data are presented as mean ± SD (n = 3). **P < 0.01, ***P < 0.001 (Student's t-test). **See also Figure S2.**

Figure 3




## Figure 3

### CHD3 Maintains Chromatin Compaction at the *PARD3B* Enhancer in SWI/SNF-Deficient Cells

**(A)** Genome browser tracks showing the occupancy of H3K4me3, H3K4me1, H3K27ac, H3K27me3, SMARCA4, and CHD3, along with ATAC-seq signals at the *PARD3B* locus in the H23 isogenic model. E1,

E2, and E3 denote putative enhancer regions where SMARCA4 and CHD3 co-localize. Note that CHD3 binding is retained in SWI/SNF-deficient (-SMARCA4) cells.

**(B)** Genome browser tracks of ATAC-seq signals at the *PARD3B* locus in SWI/SNF-deficient H23 cells treated with siNT or siCHD3. The orange box highlights the 5' enhancer region (E1) where *CHD3*depletion leads to a marked increase in chromatin accessibility, indicating transcriptional derepression. **See also Figure S3.**

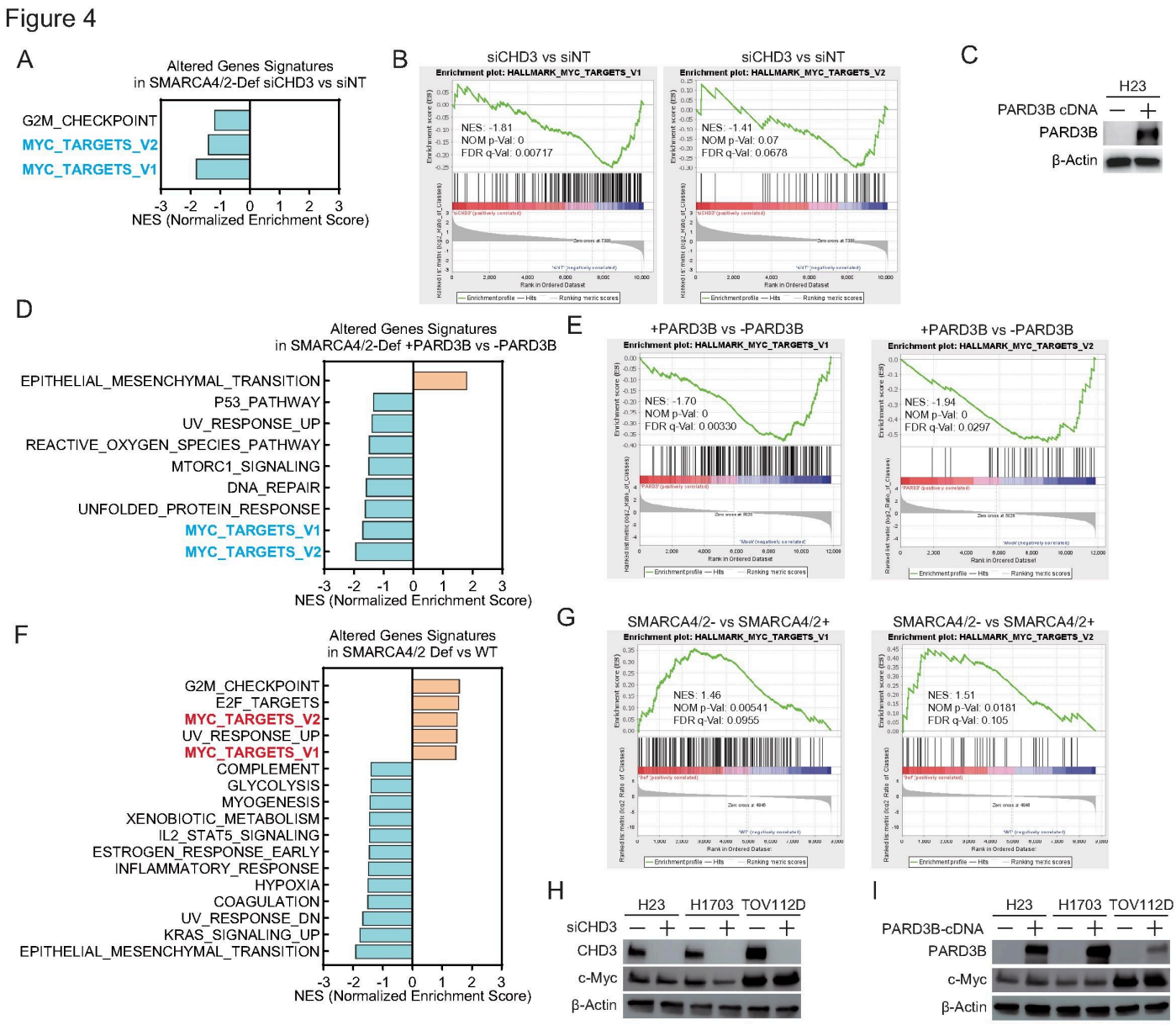



**Figure 4**

## PARD3B Accumulation Induces Functional Uncoupling of MYC Signaling

**(A)** Normalized Enrichment Scores (NES) of hallmark gene sets significantly altered in H23 cells upon *CHD3*knockdown (siCHD3) compared to control (siNT). Note the suppression of MYC target signatures.

**(B)** Gene Set Enrichment Analysis (GSEA) plots showing significant suppression of *HALLMARK_MYC_TARGETS_V2* and *V1*signatures in H23 cells upon *CHD3* knockdown (siCHD3) compared to control (siNT).

**(C)** Immunoblot confirmation of PARD3B overexpression (OE) in H23 cells transfected with a PARD3B-cDNA vector.

**(D)** Normalized Enrichment Scores (NES) of hallmark gene sets significantly altered in H23 cells upon PARD3B OE. Note the suppression of MYC target signatures.

**(E)** GSEA plots showing suppression of *HALLMARK_MYC_TARGETS_V1*(left) and *V2* (right) signatures in H23 cells upon PARD3B OE.

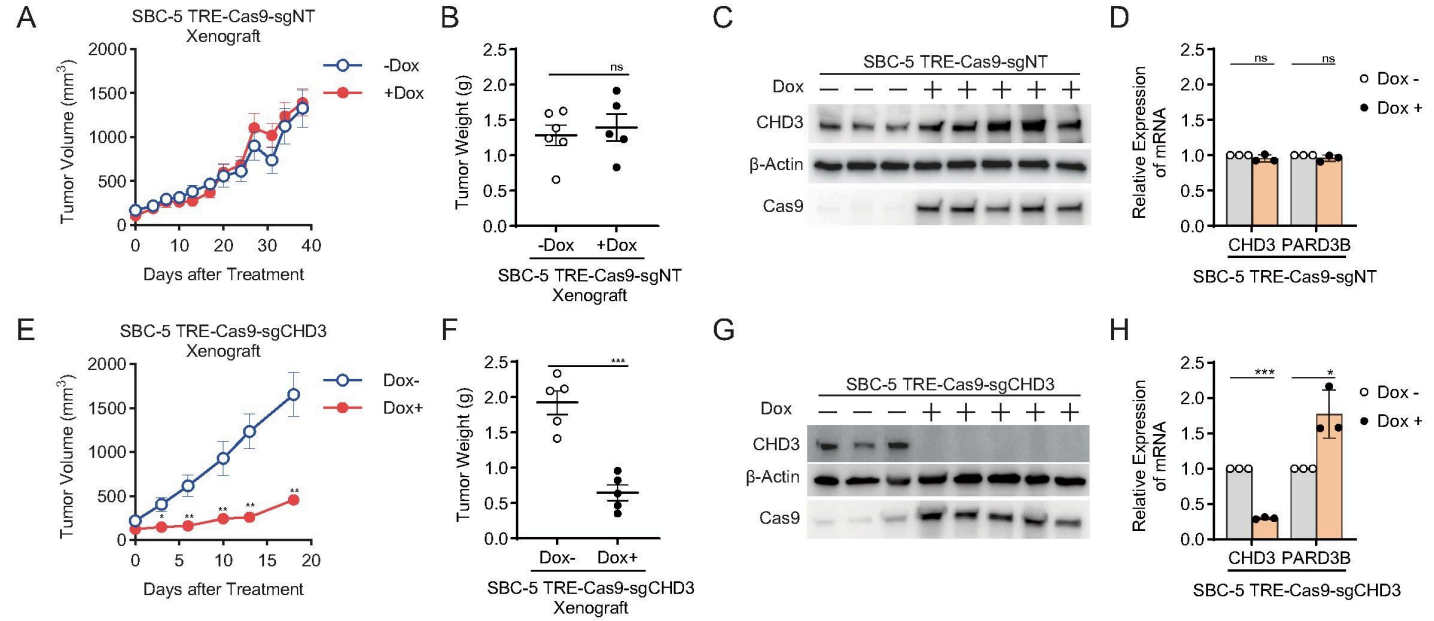
**(F)** NES of hallmark gene sets significantly enriched in SWI/SNF-deficient cells (H1703) compared to SWI/SNF-proficient cells (H2009). MYC target signatures are among the top upregulated pathways.

**(G)** GSEA plots showing enrichment of *HALLMARK_MYC_TARGETS_V1*(left) and *V2* (right) signatures in SWI/SNF-deficient cells compared to proficient cells.

**(H, I)** Immunoblot analysis of c-MYC protein in SWI/SNF-deficient cell lines (H23, H1703, TOV112D) treated for 96 h with siNT vs. siCHD3 **(H)** or Mock vs. PARD3B-cDNA **(I)**. Paradoxically, c-MYC protein levels remain stable despite the transcriptional suppression of its targets.

Data are presented as mean ± SD. **P < 0.01, ***P < 0.001. **See also Figure S4.**

Figure 5




## Figure 5

### CHD3 Depletion Induces Tumor Regression and Mechanism Validation In Vivo

**(A, B)** Tumor growth curves **(A)** and final tumor weights **(B)**of SBC-5 xenografts expressing Dox-inducible Cas9 and non-targeting sgRNA (sgNT). Mice were treated with vehicle (-Dox: n=6) or Doxycycline (+Dox: n = 5). No significant differences were observed. Data are presented as mean ± SEM. n.s., not significant.

**(C)** Immunoblot analysis of CHD3 and Cas9 expression in sgNT tumors harvested at the endpoint. β-Actin served as a loading control.

**(D)** Relative mRNA expression levels of *CHD3* and *PARD3B*in SBC-5-sgNT xenograft tumors treated with (Dox+) or without (Dox−) doxycycline. Data are presented as mean ± SD (n = 3). ns, not significant (two-tailed Student's *t*-test).

**(E, F)** Tumor growth curves **(E)** and final tumor weights **(F)**of SBC-5 xenografts expressing Dox-inducible Cas9 and *CHD3*-targeting sgRNA (sgCHD3). Mice were treated with vehicle (-Dox: n=5) or Doxycycline (+Dox: n = 5). Note the robust tumor regression induced by Dox treatment. Data are presented as mean ± SEM. *P < 0.05, **P < 0.01, ***P < 0.001 (Student's t-test).

**(G)** Immunoblot analysis of CHD3 and Cas9 expression in sgCHD3 tumors. Effective depletion of CHD3 protein upon Cas9 induction (+Dox) is confirmed. β-Actin served as a loading control.

**(H)** Relative mRNA expression levels of *CHD3* and *PARD3B*in SBC-5-sgCHD3 xenograft tumors treated with or without doxycycline. Note the significant upregulation of *PARD3B* expression following

*CHD3*depletion. Data are presented as mean ± SD (n = 3). *P < 0.05, **P < 0.01, ***P < 0.001 (two-tailed Student's *t*-test).

## Supplementary Files

This is a list of supplementary files associated with this preprint. Click to download.

- SupplementaryFigure1234S4S2CHD3SnPO260211.pdf
- SupplementaryTableS4S2CHD3SnPO260211.pdf
- SupplementaryFigurecaptions.docx